


Combined effects of thermal perturbation and in-situ stress on heat transfer in fractured geothermal reservoirs

Journal Article**Author(s):**

Sun, Zhixue; Jiang, Chuanyin; Wang, Xiaoguang; Zhou, Wen; [Lei, Qinghua](#) 

Publication date:

2021-05

Permanent link:

<https://doi.org/10.3929/ethz-b-000465300>

Rights / license:

[In Copyright - Non-Commercial Use Permitted](#)

Originally published in:

Rock Mechanics and Rock Engineering 54(5), <https://doi.org/10.1007/s00603-021-02386-2>

18 quantitatively analyze the influence of geomechanical boundary constraints and initial reservoir
19 temperature on the evolutionary behavior of fracture aperture, fluid flow and heat transfer, and further
20 identify the underlying mechanisms dominating the coupled THM processes. The results reveal that, apart
21 from enhancing normal opening of fractures, the transient cooling effect of thermal front may trigger shear
22 dilations under the anisotropic in-situ stress condition. It is found that the applied in-situ stress tends to
23 impose a strong impact on the spatial and temporal variations of fracture apertures and flow rates, and
24 eventually affect heat transfer. The enhancement of reservoir transmissivity during transient cooling tends
25 to be significantly overestimated if the in-situ stress effect is not incorporated, which may lead to unrealistic
26 predictions of heat extraction performance. Our study also provides physical insights into a fundamental
27 thermo-poroelastic behavior of fractured rocks, where fracture aperture evolution during heat extraction
28 tends to be simultaneously governed by two mechanisms: (i) thermal expansion-induced local aperture
29 enlargement and (ii) thermal propagation-induced remote aperture variation (can either increase or
30 decrease). The results from our study have important implications for optimizing heat extraction efficiency
31 and managing seismic hazards during fluid injections in geothermal reservoirs.

32 **Keywords:** thermal stress; in-situ stress; shear dilation; heat transfer; fracture network; aperture variation

33 **1. Introduction**

34 Geothermal energy stored in hot dry rocks has long been considered as an energy source alternative to
35 traditional fossil fuels. Heat extraction in geothermal reservoirs is primarily achieved by circulating cold
36 water between injection and production wells through fracture networks, which have been artificially
37 created and/or enhanced by applying various stimulation techniques. As the development of geothermal
38 reservoirs by the transient cooling scheme proceeds, the impedance to flow is decreased. The main
39 mechanisms responsible for such a behavior is the complex interaction among pore fluid pressure, rock
40 mass temperature and mechanical deformation of both fractures and reservoir matrix caused by the fluid

41 injection. The increased pore pressure and transient cooling induce matrix contraction and cause increased
42 fracture apertures. Due to the presence of natural fractures, the thermal stress and pore pressure are often
43 spatially highly variable within the reservoir. The resulting heterogeneous stress field can lead to non-
44 uniform evolution of hydraulic transmissivity and cause flow anisotropy and channeling in the reservoir.
45 To quantitatively characterize the heat extraction process in geothermal reservoirs, a numerical model that
46 can solve coupled thermal-hydro-mechanical (THM) processes is needed.

47 The numerical methods for simulating such problems can be categorized as continuum and
48 discontinuum models. The conventional continuum models treat a fractured rock as either an equivalent
49 porous medium (Y. S. Wu, 1999) or a superposition of two continua (Pruess & Narasimhan, 1985),
50 representing the combined matrix and fracture systems. Because of its simplicity and computational
51 efficiency, these models have been widely used in the analysis of field-scale heat extraction processes.
52 However, they cannot adequately consider the sharp permeability contrast between fractures and matrix,
53 the effect of local stress variation, the connectivity of large fractures and the interaction among multiple
54 discrete fractures. On the other hand, in the discontinuum model, the fractured rock is treated as an
55 assemblage of discrete fractures embedded within the rock matrix. Because the fracture geometries are
56 explicitly represented, such a discontinuum model can well capture many important hydro-mechanical
57 behaviors of fractures such as compression-induced closure and shear-induced dilation as well as resulting
58 permeability variation in complex fracture networks (Lei et al., 2017).

59 Extensive studies based on discrete fracture networks have been conducted to model the THM behavior
60 of fractured rocks (Ghassemi & Zhou, 2011; Salimzadeh et al., 2018), and have shown that transient cooling
61 and fluid overpressure lead to a reduction in effective stress and an increase in fracture transmissivity. The
62 THM coupling can result in faster thermal drawdown comparing to heat extraction simulations with the
63 mechanical effect omitted (Hicks et al., 1996). It has been observed that the poro-elastic effect plays a
64 dominant role in fracture aperture evolution only over short time scales (~ a few days) whereas the thermo-
65 elastic effect influences the aperture evolution during the entire production phase over long time scales (e.g.
66 a few years) (Ghassemi & Zhou, 2011). Moreover, fracture aperture heterogeneity was found to cause flow

67 channelization and extra thermal drawdown (Guo et al., 2016). Such effect is stronger if the aperture
68 correlation length is larger. Other material and operational parameters such as fracture stiffness, thermal
69 expansion coefficient, injection temperature, and injection rate may also introduce additional effects on the
70 fracture aperture evolution (Pandey & Vishal, 2017; S. Wang et al., 2016). Nevertheless, these previous
71 studies were mainly based on thermal drawdown curves, which only represent the bulk behavior of the
72 geothermal system.

73 A few recent studies have investigated the evolution of fracture transmissivity or aperture in fracture
74 clusters (Vik et al., 2018; Zhao et al., 2015) or discrete fracture networks (Fu et al., 2016; Gan & Elsworth,
75 2016; Han et al., 2019; Koh et al., 2011; Sun et al., 2017; Yao et al., 2018). These studies suggest that the
76 thermal stress tends to have a dominant role in increasing fracture permeability, which is responsible for
77 the enhanced flow channelization and faster thermal drawdown (Fu et al., 2016). The channelized flow and
78 anisotropic heat transfer behavior are found to be controlled by fracture characteristics such as length and
79 orientation (Han et al., 2019; Sun et al., 2017). These previous studies have mostly focused on analyzing
80 the fracture aperture evolution either caused by thermal stresses, whilst the combined effects of thermal and
81 in-situ stresses remain poorly elucidated, especially for complex discrete fracture networks. Such
82 limitations hinder our fundamental understanding of the THM behavior of geothermal reservoirs during
83 thermal extraction.

84 In this work, we study this issue using high-fidelity numerical modeling of coupled geomechanics, fluid
85 flow and heat transfer in 2-D fractured rocks. Here, we approximate the 3D system using a 2-D model
86 assuming a plane-strain condition, which is considered to be a reasonable assumption for the deeply buried
87 geological formation here. We specifically focus on investigating how the transient thermal perturbation
88 and in-situ stress mutually interact with each other and how their combined effects affect geothermal
89 reservoir performance. The effect of in-situ stresses was considered in many previous studies on THM
90 modelling (Sun et al., 2017; Yao et al., 2018). We show that in-situ stress loading may induce significant
91 impact on heat transfer in two-dimensional (2D) heterogeneous fracture networks. Ignoring such an effect
92 may exaggerate the enlargement of fracture apertures during the transient cooling process, resulting in

93 biased predictions of the heat transfer behavior and heat production performance of the reservoir, e.g., heat
94 breakthrough and thermal drawdown.

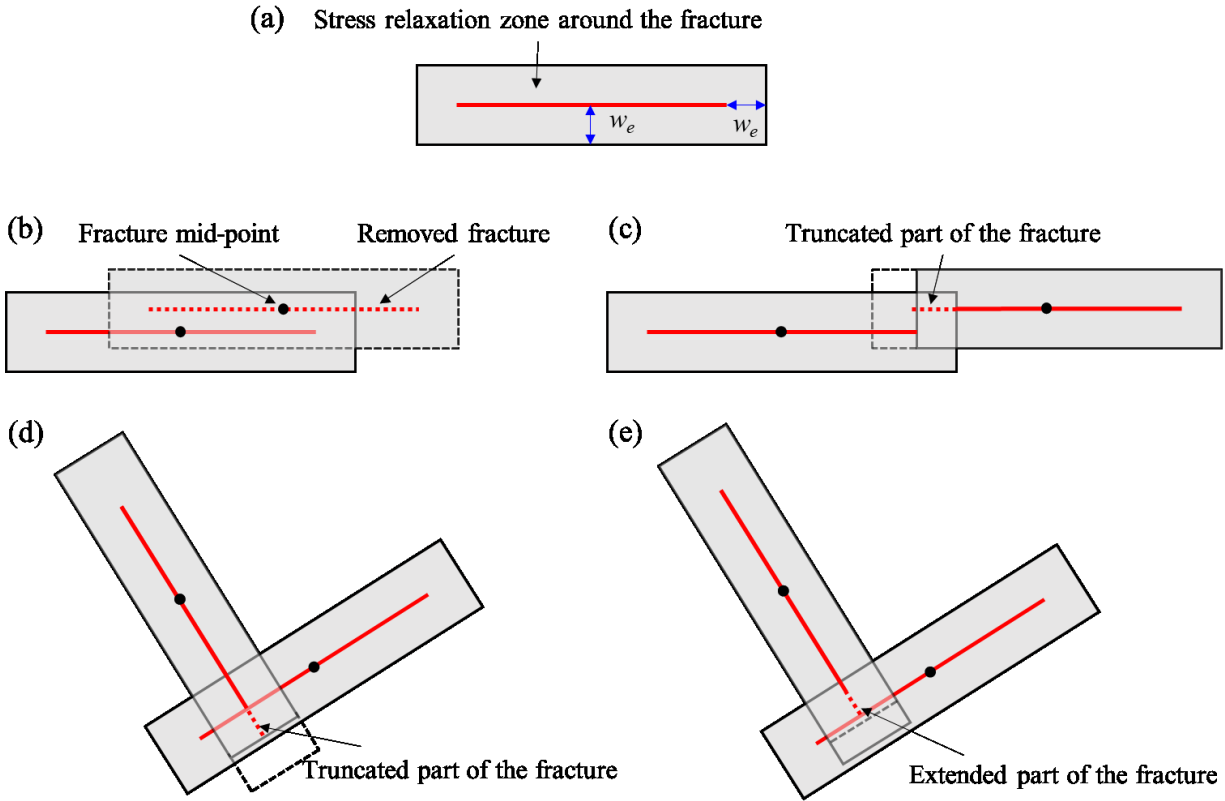
95 In a recent study, we have shown that anisotropic confining stresses can lead to anomalous heat
96 transport in fracture networks (Sun et al., 2020). However, thermal stress induced by transient cooling due
97 to thermo-poroelastic effects was not included in that study. In this work, we develop a fully-coupled THM
98 model to investigate the complex interaction between thermal and in-situ stresses, and elucidate their
99 coupled effects on fracture aperture evolution during the heat extraction process. Our model takes into
100 account compression-induced closure, shear-induced dilation and thermal-induced opening of fracture
101 apertures. The results provide important insights into the dynamic evolutionary behavior of the fracture
102 aperture field during transient cooling, which are useful for optimizing thermal extraction strategies for
103 geothermal reservoirs. The remainder of the paper is organized as follows. In Section 2, the fully-coupled
104 THM numerical model is introduced. Section 3 describes the model setup and simulation procedure with
105 the results further presented in Section 4. Finally, in Section 5, some discussions and concluding remarks
106 are provided.

107 **2. Numerical methods**

108 2.1 Discrete fracture network generation

109 The 2D discrete fracture network (DFN) used in this work is generated with the fracture lengths
110 following a lognormal distribution which has been observed in many outcrops of real fracture systems
111 (Einstein & Baecher, 1983; Hudson & Priest, 1983). Laboratory experiments (Rives et al., 1992; H. Wu &
112 Pollard, 1995), numerical simulations (Bai et al., 2000; Carl E Renshaw & Pollard, 1994; Rives et al., 1992;
113 H. Wu & Pollard, 1995) and field observations (C. E. Renshaw & Park, 1997) have shown that the evolution
114 of fracture spacing is governed by the mechanical interaction between emerging/growing fractures. To
115 consider this important mechanical interaction among fractures, the concept of a stress shadow (or
116 relaxation) zone around pre-existing fractures is implemented in our DFN model to mimic this effect in a
117 statistical framework (Wang et al., 2017).

118 By integrating the shadow zone model into the random fracture network generation process, the self-
119 organized geometries and topologies of natural joint systems can be more realistically represented. A 2D
120 DFN model can be created by the following steps. (1) Randomly choose a point as the mid-point of a new
121 fracture. If the seed is located within the shadow zone of an existing fracture, remove this seed and
122 regenerate a new one (Figure 1b). (2) Assign a random length value drawn from the predefined length
123 distribution (i.e., lognormal function here) for the new fracture. Assign an orientation value drawn from the
124 predefined orientation distribution (i.e., two orthogonal orientations here) for the new fracture. If the
125 fracture intersects with the shadow zone of other pre-existing fractures, it will be truncated (Figure 1c). If
126 the fracture's shadow zone overlaps that of an existing orthogonal fracture, it is either truncated (Figure 1d)
127 or extended (Figure 1e) so that the new fracture abuts the old one. (3) A new stress shadow zone is also
128 assigned to the most recently generated fracture to constrain the generation of subsequent ones. This
129 procedure is iterated until the fracture network reaches the target intensity. The fracture spacing is not pre-
130 defined, but is controlled by the statistical distribution of fracture mid-points, lengths as well as stress
131 shadow zone parameters. The minimal possible spacing between two fractures is controlled by the half
132 width (w_e) of the fracture shadow zone (Figure 1a).



133

134 **Figure 1.** Demonstration of the generic DFN generation model. (a) A stress shadow zone around a fracture. w_e is a geometrical
 135 parameter that defines the shadow zone width. (b) If the seed of a new fracture with the same orientation to the pre-existing fracture
 136 falls into its shadow zone, the seed is removed and the new fracture will not be generated. (c) The new fracture, parallel to an
 137 existing fracture that enters into its shadow zone, is truncated. (d) The new fracture, not parallel to an existing fracture that enters
 138 into its shadow zone and cross it, is truncated. (e) The new fracture, not parallel to an existing fracture that enters into its shadow
 139 zone but does not cross it, is extended.

140 2.2 Thermal-hydraulic-mechanical (THM) coupled modeling

141 In this work, the full coupled problem of geomechanical deformation, fluid flow and heat transport in
 142 geothermal reservoirs is solved based on the finite element method. The model is implemented in the
 143 commercial software, COMSOL Multiphysics. The model domain is discretized using an unstructured
 144 mesh with 2-D triangular matrix elements and 1-D linear fracture elements (treated as internal interfaces).
 145 The governing equations of the THM model are described in detail as follows.

146 2.2.1 Geomechanical deformation

147 The fractured rock in the geothermal reservoir is modeled as a combination of high-permeability
 148 fractures and a low-permeability rock matrix that surround the fractures. Because the magnitude of matrix
 149 permeability in hot dry rocks is significantly lower than that of fractures, the flow pathways tend to be
 150 controlled by fractures. We model the deformability of fractures under normal compression based on a
 151 hyperbolic model (Bandis et al., 1983; Barton et al., 1985):

$$152 \quad v_n = \frac{\sigma_n v_m}{K_{n0} v_m + \sigma_n} \quad (1)$$

153 where the v_n is the normal closure, K_{n0} is the initial normal stiffness, v_m is the maximum allowable closure,
 154 and σ_n is the effective normal compressive stress which is equal to the difference between the total normal
 155 stress on the fracture and the fluid pressure inside the fracture.

156 The shear deformation is calculated based on the excess shear stress concept (Rahman et al., 2002;
 157 Ucar et al., 2017). The excess shear stress, $\Delta\tau$, is defined as the difference between the shear stress and
 158 shear strength on the fractures:

$$159 \quad \Delta\tau = \tau - \sigma_n \tan\phi \quad (2)$$

160 where τ is the shear stress and ϕ is the friction angle. For a fracture with its shear stress exceeding the yield
 161 surface of the Mohr-Coulomb criterion, the shear displacement, u_s , is approximated by dividing the excess
 162 shear stress by the shear stiffness, K_s , such as in linear elastic theory (Rahman et al., 2002; Ucar et al., 2017):

$$163 \quad u_s = \frac{\Delta\tau}{K_s} \quad (3)$$

164 Ultimately, the dilational displacement v_s is related to the shear displacement u_s via an incremental form as
 165 (Saeb & Amadei, 1992):

$$166 \quad v_s = -u_s \tan\phi_i \quad (4)$$

167 where ϕ_i is the dilation angle. The fracture aperture b under coupled normal and shear loadings is thus given
 168 by (Lei et al., 2016):

$$169 \quad b = \begin{cases} b_0 + w, & \sigma_n < 0 \\ b_0 - v_n - v_s, & \sigma_n \geq 0 \end{cases} \quad (5)$$

170 where b_0 is the initial aperture, and w is the separation of opposing fracture walls if the fracture is under
 171 tension.

172 The mechanical deformation of rock matrix is modeled based on thermo-poro-elasticity principles
 173 (Jaeger et al., 2009). By synthesizing the effect of thermal expansion and pore pressurize, the governing
 174 equation for the matrix deformation is written as (Zhao et al., 2015):

$$175 \quad \sigma'_{ij} = \sigma_{ij} - \alpha_B p \delta_{ij} = \frac{Ev}{(1+\nu)(1-2\nu)} \varepsilon_{ki} \delta_{ij} + \frac{E}{1+\nu} \varepsilon_{ij} - \frac{E}{1-2\nu} \alpha_T \Delta T \delta_{ij} \quad (6)$$

176 where σ'_{ij} is the effective stress, ε_{ij} is the strain, E is the Young's modulus, ν is the Poisson's ratio, α_B is the
 177 Biot's coefficient, p is the fluid pressure, δ_{ij} is the Kronecker delta, α_T is the thermal expansion coefficient
 178 and ΔT is the temperature increment defined as $\Delta T = T - T_{ref}$ with T and T_{ref} being the rock and reference
 179 temperatures, respectively.

180 2.2.2 Fluid flow

181 Single-phase flow of compressible fluids through fractured porous media is governed by the following
 182 mass conservation and momentum equations for matrix and fracture elements:

$$183 \quad \varepsilon \chi_f \frac{\partial p}{\partial t} + \nabla \cdot (\mathbf{u}_m) = 0, \quad (7)$$

$$184 \quad \mathbf{u}_m = - \frac{\kappa_m}{\mu} \nabla p, \quad (8)$$

185 and

$$186 \quad b \chi_f \frac{\partial p}{\partial t} + \nabla_\tau \cdot (b \mathbf{u}_f) = f_{up} + f_{bottom}, \quad (9)$$

$$187 \quad \mathbf{u}_f = - \frac{\kappa_f}{\mu} \nabla_\tau p, \quad (10)$$

188 where \mathbf{u} is the velocity vector and κ is the permeability with the subscripts 'm' and 'f' denoting the matrix
 189 and fractures, respectively, ε is the matrix porosity, p is the pressure, t is the time, μ is the fluid dynamic
 190 viscosity and χ_f is the fluid compressibility, $f_i = - \frac{\kappa_m}{\mu} \frac{\partial p_i}{\partial n_i}$ is the fluid exchange term between fracture and
 191 matrix, with subscript 'i' representing the up and bottom matrix blocks from two sides of the fracture and

192 n_i representing the outward normal direction of the matrix. ∇_τ denotes the gradient operator restricted to the
 193 fracture's tangential plane. The fracture permeability κ_f is calculated using the cubic law based on stress-
 194 dependent fracture aperture. The local permeability is assumed to be constant for all matrix elements.

195 2.2.3 Heat transfer

196 The energy conservation equations describing the heat transfer process in the fractured rock are given
 197 below. In the rock matrix, the energy conservation equation is described as:

$$198 \quad (\rho C)_{eff} \frac{\partial T}{\partial t} + \rho_f C_f \mathbf{u}_m \cdot \nabla T + \nabla \cdot (-\lambda_{eff} \nabla T) = 0, \quad (11)$$

199 where $(\rho C)_{eff} = \varepsilon \rho_f C_f + (1 - \varepsilon) \rho_s C_s$ and $\lambda_{eff} = \varepsilon \lambda_f + (1 - \varepsilon) \lambda_s$ are the effective heat capacity and the
 200 effective thermal conductivity, respectively, obtained through volume averaging, T is the temperature, ρ is
 201 the density, C is the specific heat capacity, and λ is the heat conductivity with the subscripts 's' and 'f'
 202 denoting the rock solid and fluid phases, respectively.

203 In discrete fractures, the energy conservation equation is given as:

$$204 \quad b \rho_f C_f \frac{\partial T}{\partial t} + b \rho_f \mathbf{u}_f C_f \nabla_\tau T_f - \nabla_\tau \cdot (b \lambda_f \nabla_\tau T) = e_{up} + e_{bottom}, \quad (12)$$

205 where e_{up} and e_{bottom} are the energy exchange terms between fractures and matrix. Up and bottom stand for
 206 matrix from different sides of the fracture, such that $e_i = \rho_f C_f T_i \cdot f_i - \lambda_{eff} \frac{\partial T_i}{\partial n_i}$ with i meaning up or bottom.

207 In this study, the relative production temperature is defined as a normalized formulation:

$$208 \quad T^* = \frac{T_{out} - T_0}{T_{in} - T_0}, \quad (13)$$

209 where T_{out} and T_{in} are the fluid temperatures at the production and injection wells, respectively; T_0 is the
 210 initial temperature of the reservoir. To further quantify the timescales of convective and conductive
 211 transport processes, we introduce a dimensionless quantity as (Sun et al., 2020):

$$212 \quad R = \frac{2\varepsilon_m D_m}{\bar{u}_f \bar{d}_f}, \quad (14)$$

213 where $\varepsilon_m = \varepsilon + (1 - \varepsilon) \frac{\rho_s C_s}{\rho_f C_f}$, \bar{d}_f is the mean fracture aperture, \bar{u}_f is the mean fracture velocity and

214 $D_m = \frac{\lambda_s}{\rho_s C_s}$ is the heat diffusion coefficient in the matrix. Note that the heat transfer in the matrix is

215 dominant by diffusion since the matrix permeability is significantly small. R can be thought as the inverse
216 of a fracture-matrix Péclet number, and it represents a ratio of convection to conduction timescales.

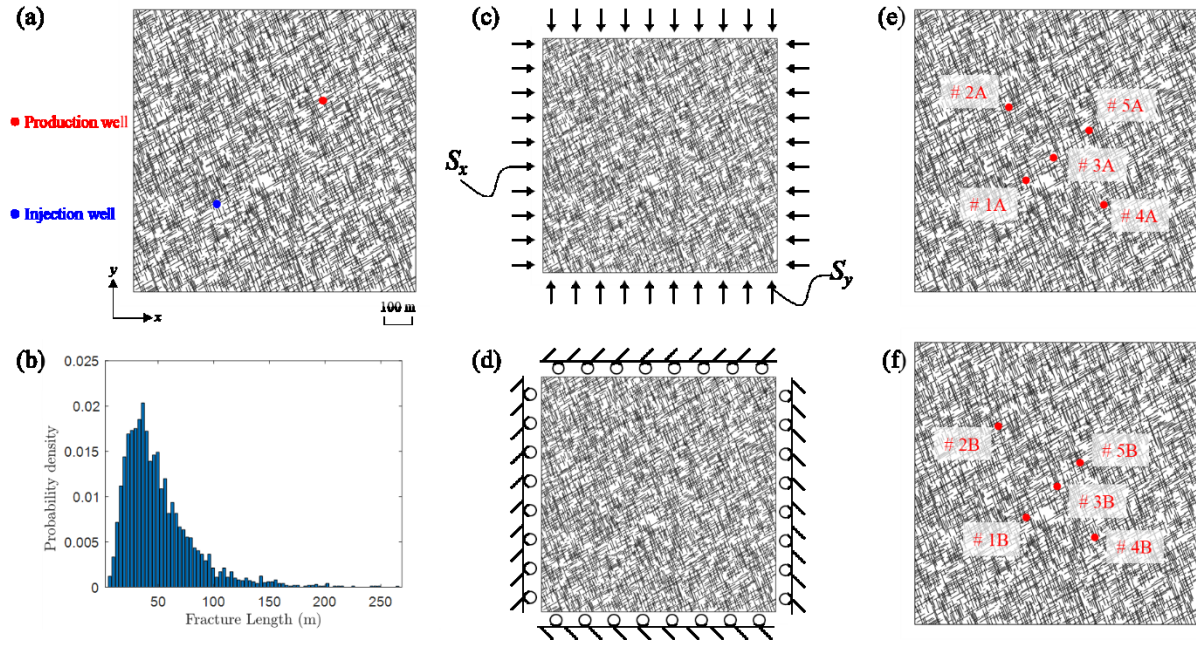
217 3. Numerical model setup

218 As shown in Figure 2a, the modeled area has a dimension of 1000 m \times 1000 m with 3000 fractures.
219 The DFN consists of two fracture sets with fixed orientations of 30° and 110°. The fracture trace length
220 follows a lognormal distribution with a mean value of 30 m and a variance of 0.6 (Figure 1b). The
221 stochastically generated fracture network, is well connected and shows a strong geometrical anisotropy.
222 Such a simple DFN is chosen as it preserves the essential geometrical features of the geothermal reservoir,
223 allowing us to focus on investigating the complex THM responses of the fractured geothermal reservoirs
224 in a generic perspective.

225 We consider the target reservoir at a depth of 3000 m. The overburden stress is $S_v = 79.83$ MPa
226 assuming the rock density is 2700 kg/m³. We apply horizontal in-situ stresses S_x and S_y , along the x - and y -
227 directions, respectively, and orthogonally to the domain (Figure 2c). We denote the ratio of the horizontal
228 stresses to the vertical stress as $k_x = S_x/S_v$ and $k_y = S_y/S_v$ and explore three different scenarios: (i) $k_x = 0.8$, k_y
229 $= 0.8$; (ii) $k_x = 0.8$, $k_y = 1.6$; (iii) $k_x = 1.6$, $k_y = 0.8$. Another set of simulations with displacement boundary
230 constraints are also performed, where a roller condition is assumed for all model boundaries (Figure 2d).
231 Such a roller boundary has been adopted by many previous studies without considering in-situ stresses and
232 we will investigate the consequences based on a comparative analysis. A constant initial aperture of 0.4
233 mm is assigned to all fractures. For the cases applied with stress boundary constraints, an equilibrium state
234 regarding pore pressure, temperature and stress fields is first achieved within the entire reservoir domain
235 before modelling the heat extraction process. Then, the heat production is started at a given time and the

236 flow circulation is established by elevating the hydraulic head at the injection well to create a fixed
237 hydraulic gradient between the injection and production wells (Figure 2a). During the entire production
238 period, a no-flow condition is imposed for all domain boundaries. The boundary condition for the heat
239 transfer calculation are specified as follows: cold fluid of 20 °C is injected at the injection well when
240 reservoir operations initiates. Three initial temperatures of $T_0 = 120, 220$ and 320 °C are considered. The
241 domain boundaries are assumed to be of adiabatic type. The properties of rock and fluid as well as the initial
242 and boundary condition parameters in the coupled THM simulations are listed in Table 1 and 2. To track
243 the spatially varying aperture evolution, we set five monitoring points for each fracture set. The locations
244 of the monitoring points are shown in Figures 2e and 2f.

245 The coupled THM models were solved using COMSOL Multiphysics V5.4 (*COMSOL Multiphysics*®,
246 2018). The model domain was discretized by triangular elements. The mesh size was optimized to ensure
247 calculation accuracy whiling maintaining efficiency. The simulation is implemented by two sequential steps:
248 (1) in-situ stress initialization and (2) heat production. In the first stage, we aim to mimic the in-situ reservoir
249 condition before production. Thus, there is no pressure difference between production and injection wells,
250 i.e., the pressure in both wells equals to the reservoir pressure. The simulation time in this step was set as
251 2×10^9 s (≈ 63 a) which is long enough to attain an equilibrium state of stress under the combined effect of
252 in-situ stresses, thermal stress induced by initial reservoir temperature and the initial pore pressure of the
253 reservoir. At the time of 2×10^9 s, gradients of pressure (from p_0 to p_{in}) and temperature (from T_0 to T_{in}) were
254 established, which indicates the beginning of heat production. The production duration was set to 10^{11} s for
255 all cases which is enough to extract all heat of the reservoir. Besides, the logarithmic time stepping strategy
256 was adopted to capture the short-time variation of temperature fields. Note that in the text below, the
257 production time refers to the time after the initialization time 2×10^9 s.



258

259

260

261

Figure 2. (a) The 2D discrete fracture network used in the coupled THM simulation. (b) The length distribution of the discrete fracture network. (c) Schematic showing the stress boundary condition. (d) Schematic showing the roller boundary condition. (e) Layout of monitoring points on the 110° fracture set. (f) Layout of monitoring points on the 30° fracture set.

262 **Table 1.** The rock and fluids properties used in the coupled THM simulation

Rock matrix parameters			
Rock density	ρ_s	kg/m ³	2700
Porosity	ε	-	0.0001
Poisson's ratio	ν	-	0.25
Young's modulus	E	GPa	30
Biot's coefficient	α_B	-	1
Thermal expansion coefficient	α_T	1/K	3×10^{-6}
Reference temperature	T_{ref}	°C	20
Matrix permeability	κ_m	m ²	1×10^{-18}
Matrix heat capacity	C_s	J/(kg·K)	1000
Matrix heat conductivity	λ_s	W/(m·K)	3
Fracture parameters			
Initial aperture	b_0	m	4×10^{-4}
Fracture permeability	κ_f	m ²	$b^2/12$
Maximum possible closure	ν_m	m	$0.8b_0$
Fracture initial normal stiffness	K_{n0}	GPa/m	50
Fracture shear stiffness	K_s	GPa/m	10
Fracture dilation angle	ϕ_i	°	10
Fracture friction angle	ϕ	°	31
Fluid parameters			
Fluid compressibility	χ_f	1/Pa	5×10^{-10}
Fluid density	ρ_f	kg/m ³	1000
Fluid viscosity	μ	Pa·s	5×10^{-4}
Fluid heat capacity	C_f	J/(kg·K)	4200
Fluid heat conductivity	λ_f	W/(m·K)	0

263 **Table 2.** The initial and boundary condition parameters used in the coupled THM simulation

Initial condition parameters			
Gravity acceleration	g	m ² /s	9.8
Reservoir depth	H	m	3000
Initial reservoir pressure	p_0	Pa	$\rho_f g \cdot H$
Initial Temperature	T_0	°C	120, 220, 320
Domain length	L	m	300
Boundary condition parameters			
Vertical stress	S_v	Pa	$\rho_s \cdot g \cdot H$
Ratio of x-direction horizontal to vertical stresses	k_x	-	0.8, 0.8, 1.6
Ratio of y-direction horizontal to vertical stresses	k_y	-	0.8, 1.6, 0.8
x-direction horizontal stress	S_x	Pa	$k_x \cdot S_v$
y-direction horizontal stress	S_y	Pa	$k_y \cdot S_v$
Production pressure	p_{out}	Pa	p_0
Injection pressure	p_{in}	Pa	$p_{out} + 10 \text{ MPa}$
Injection water temperature	T_{in}	°C	20

264 **4. Results**

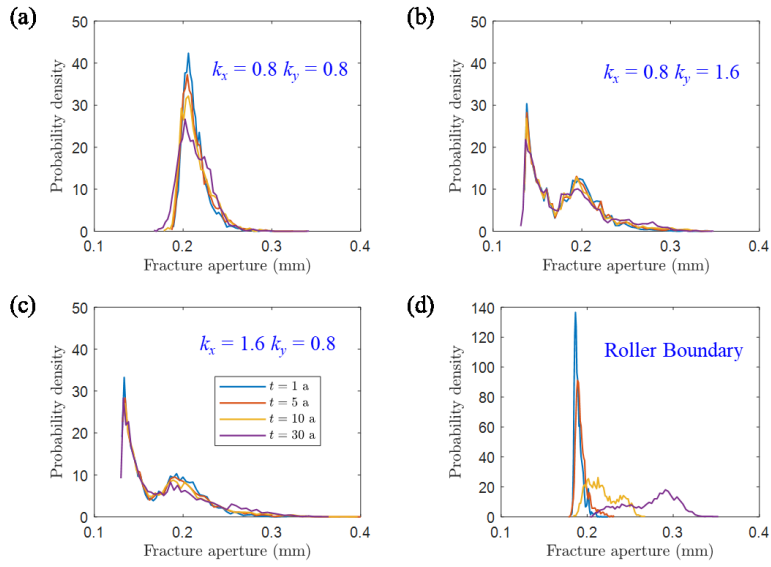
265 4.1 Results of geomechanical deformation

266 Figure 3 shows the probability density functions (PDFs) of fracture apertures at selected four
267 production times under different geomechanical boundary conditions. Figure 4 presents the corresponding
268 heterogeneous distributions of fracture apertures for respective cases. The results presented in both figures
269 are for the initial temperature condition of $T_0 = 220$ °C. At the initial stage of heat extraction (i.e., $t = 1$ a),
270 the Gaussian-like aperture distribution for the case under an isotropic stress loading (Figure 3a) is similar
271 to that of the roller boundary case (Figure 3d). This is because the cold front only affects the area around
272 the injection well at early times (Figure 4) such that the deformation of fractures in the two cases are
273 dominated by compression-induced normal closure. When an anisotropic far-field stress is applied (Figures
274 3b and 3c), the aperture PDFs exhibit a bimodal form with the two peaks corresponding to the two different
275 fracture sets. This is because the two fracture sets at different orientations with respect to the in-situ stress
276 loading tend to accommodate different normal and shear stresses, as expected from the Mohr's circle stress
277 solution (Jaeger et al., 2009), such that the two fracture sets exhibit different aperture values. In addition,
278 the second peak of the case of $k_x = 1.6$ and $k_y = 0.8$ is slightly shifted towards large aperture values
279 comparing to the case of $k_x = 0.8$ and $k_y = 1.6$. This is caused by the intrinsic geometrical heterogeneity of
280 the fracture pattern, which accommodates more shear displacements and dilations in the former case.

281 As the reservoir development proceeds (e.g., $t = 5$ a and 10 a), the aperture PDFs of cases where
282 anisotropic in-situ stresses are applied (Figures 3b and 3c) exhibit a mild change comparing to that at $t =$
283 1a. The bimodal form is maintained whereas the apertures of some fractures become larger, due to transient
284 cooling-induced fracture unloading that tends to alleviate normal closure under reduced normal stress and
285 also promote shear dilation under reduced shear resistance (proportional to normal stress via the friction
286 coefficient). The number of large apertures increases gradually with time as the cold front propagates
287 towards the downstream (Figure 4; rows 2 and 3). For the stress case of $k_x = 0.8$ and $k_y = 1.6$, the aperture
288 increase occurs mainly in fractures of the 110° set, whereas for the case of $k_x = 1.6$ and $k_y = 0.8$, increased
289 fracture apertures mostly happen along fractures of the 30° set. To better understand the process, we derive
290 the components contributing to the aperture variation: the amount of normal closure, v_n , shear dilation, v_s ,

291 as well as the net aperture change, $v_n + v_s$. Figure 5 presents the evolution of v_n , v_s and $v_n + v_s$ monitored at
292 the probing point 1 on the 110° fracture set when $T_0 = 220^\circ\text{C}$. It can be seen that shear dilation only occurs
293 in the case of anisotropic in-situ stresses with $k_x = 0.8$ and $k_y = 1.6$. Also, the onset of the shearing
294 corresponds to the moment when the normal closure decreases (due to cooling-induced unloading). We
295 interpret the operating mechanism as follows. When the fractured rock is subject to anisotropic in-situ
296 stresses, shear load is imposed along preferentially orientated fractures. Once the thermal front arrives, a
297 thermal stress is generated by the cooling effect, which reduces the effective normal stress acting on the
298 fracture. Consequently, the shear strength is reduced. Once the shear strength is lower than the shear stress,
299 fracture sliding would occur with dilational displacement produced.

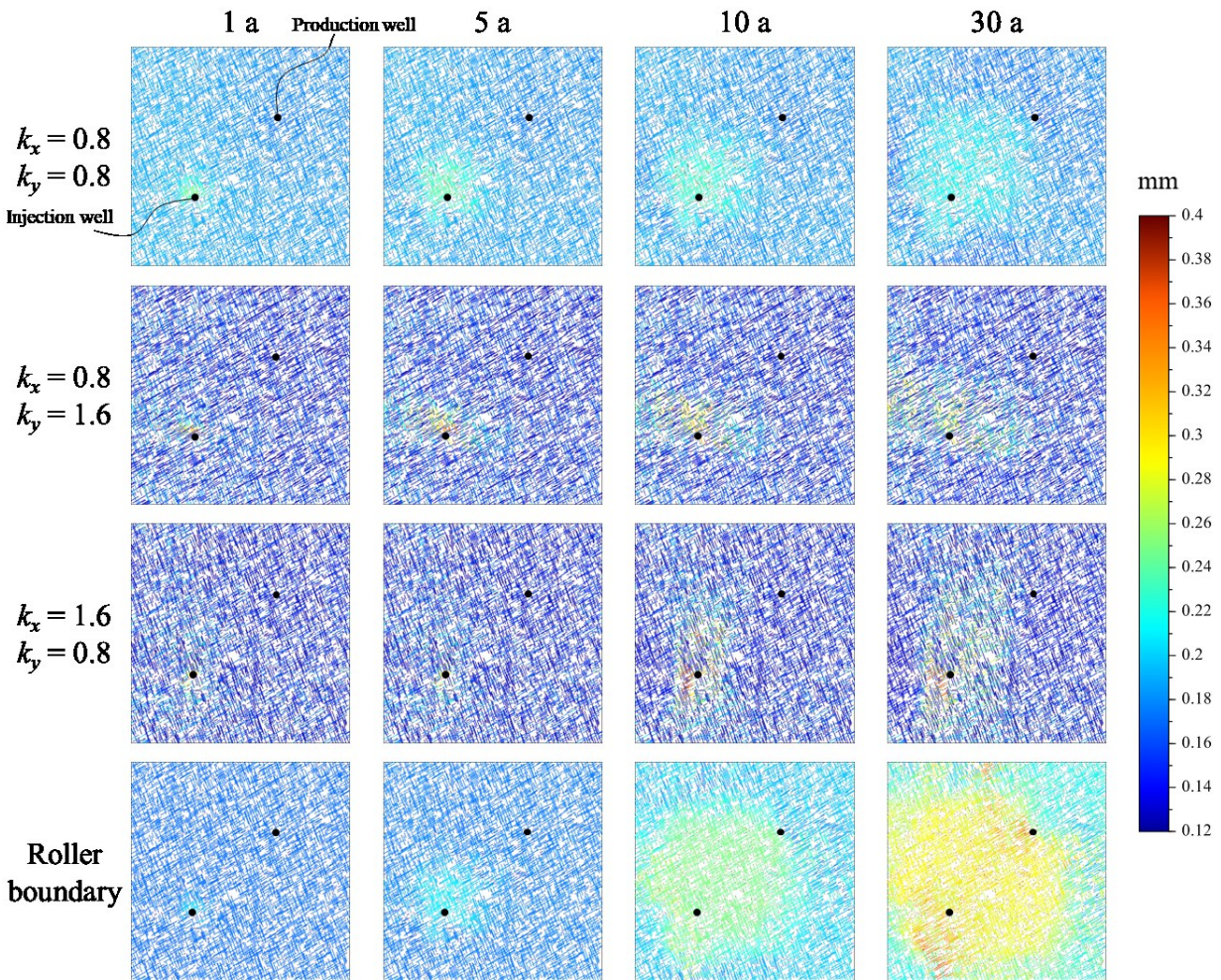
300 If the fractured rock is isotropically stressed, i.e., $k_x = 0.8$ and $k_y = 0.8$, the spread of the aperture
301 distribution is broadened at first but then tapered. The mean value tends to shift towards larger value regimes
302 as the production time increases (Figure 3a). However, the general unimodal shape of the aperture PDF is
303 kept all the time. In contrast, when the fractured rock is not subject to in-situ stresses (i.e., when roller
304 boundaries are applied), the aperture distribution changed totally with the increased time (Figure 3d). The
305 mean aperture values increase persistently over time. There is an increase of more than 1.5 times during 30
306 years of reservoir development. The manner of how the spatial distribution of fracture aperture evolves for
307 the roller boundary case is also different from that of cases subject to stress loadings (Figure 4). This clearly
308 demonstrates the impact of in-situ stresses on aperture evolution during the heat extraction. If it is neglected,
309 the value of fracture apertures tends to be overestimated. In addition, the overestimation becomes gradually
310 exaggerated as the reservoir development continues.



311

312

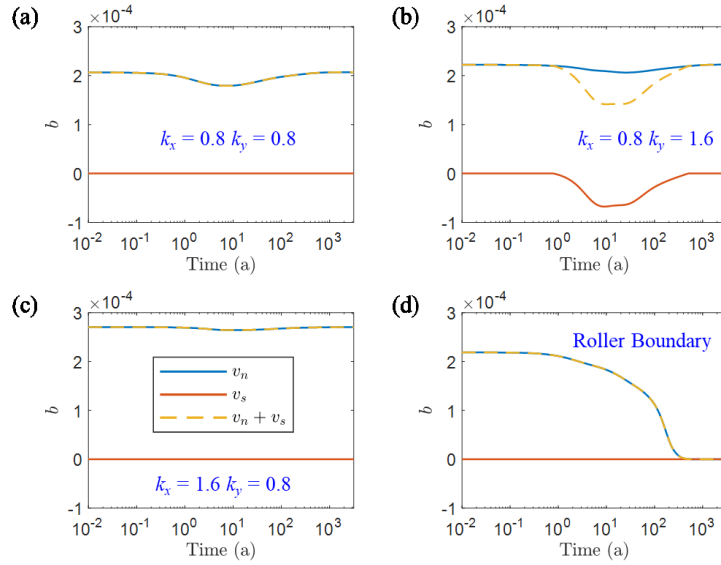
Figure 3. Aperture PDFs for various in-situ stress cases at selected four production times of 1, 5, 10 and 30 years.



313

314

Figure 4. Spatial distribution of fracture apertures for various in-situ stresses at four different production times.

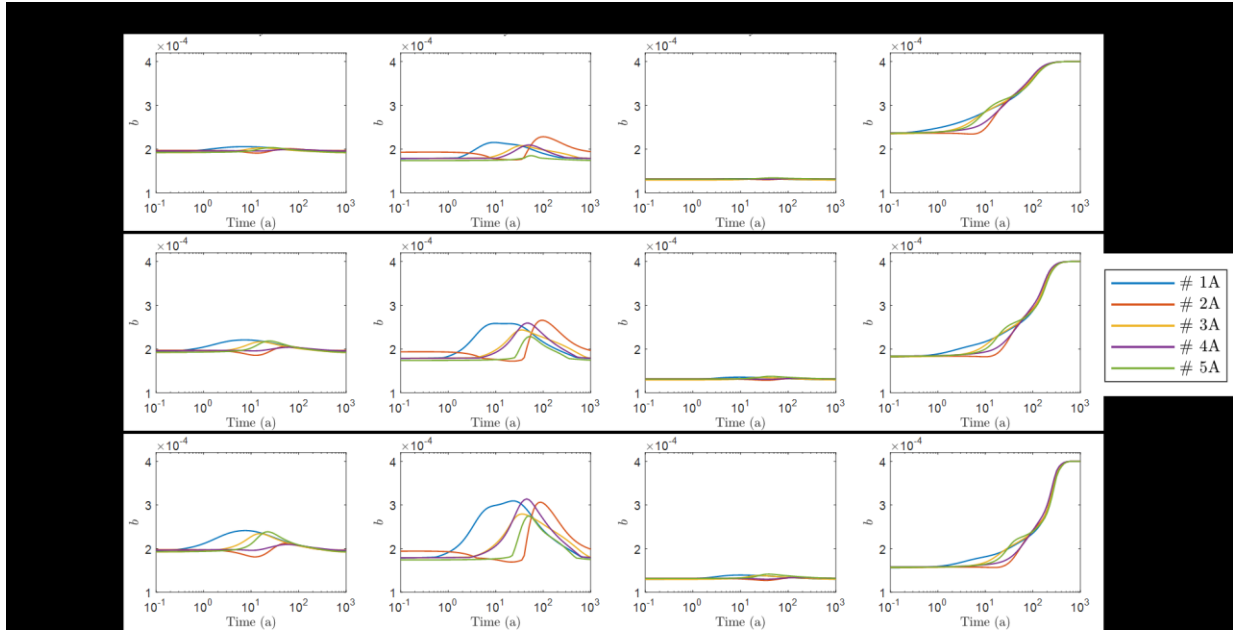


315
 316 **Figure 5.** Evolution of normal closure (v_n), shear displacement (v_s) and net aperture change ($v_n + v_s$) for sampling point 1 on 30°
 317 fracture set under (a) roller boundary condition, (b) $k_x = 0.8, k_y = 0.8$, (c) $k_x = 0.8, k_y = 1.6$, (d) $k_x = 1.6, k_y = 0.8$.

318 To further elucidate the in-situ stress effect on fracture aperture, we analyze the aperture evolution of
 319 fractures intersecting the monitoring points (Figures 2e and 2f) during the entire heat extraction period.
 320 Figures 6 and 7 present the results for the 110° and 30° fracture sets, respectively. At very early time ($t \leq$
 321 0.1 a), the cold front has not yet arrived at the monitoring points within the fracture networks. There is only
 322 a small difference in the fracture aperture behavior among these points, indicating that the pressure gradient
 323 has a minor effect on the aperture spatial distribution. After that, the curves of aperture evolution exhibit
 324 different behaviors depending on the monitoring location and in-situ stress condition. The chronological
 325 order of the aperture variation for the stress boundary cases seems to be in accordance to the relative
 326 distance between the monitoring point and the injection well along the mean flow direction (Figure 6; first
 327 row; points 1, 3, 5). Moreover, these points all exhibit a similar variation behavior: the aperture first
 328 increases and then decreases until it returns to the original value. The magnitude of the variation peak
 329 depends on the in-situ stress conditions (Figure 6; first row). For instance, the aperture variation at point 1
 330 on the 110° fracture set is milder under the stress case of $k_x = 1.6$ and $k_y = 0.8$ in comparison to the other
 331 two far-field stress cases, because the 110° set is under higher normal stress (more normal closure) and also

332 more suppressed for shearing (less shear dilation) in the case of $k_x = 1.6$ and $k_y = 0.8$. For monitoring points
333 across the mean flow direction (i.e., points 2 and 4), the aperture variation trend is more complex: a decline
334 in aperture is observed before the variation peak (Figure 6). Similar phenomena can also be observed in
335 Figure 7. However, the non-uniform thermal stress distribution due to the complex fracture geometry may
336 lead to different aperture evolution behaviors of the two fracture sets. Such a behavior implies that a fracture
337 may experience a deformation due to the stress perturbation induced by the thermal front remotely, while
338 it could undergo a second influence by the transient cooling upon the arrival of the thermal front at the
339 fracture. On the other hand, if the fractured rock is subject to roller boundaries without in-situ stress loading,
340 all fractures show a similar, simple, behavior of aperture evolution: the aperture increases consistently as
341 the transient cooling operates until reaching and then stabilizing at a maximum value. Because the reservoir
342 temperature at the end of the simulation is 20 °C, which equals to the reference temperature (T_{ref}), the
343 maximum aperture value corresponds the condition of zero thermal stress. Therefore, a higher initial
344 reservoir temperature generates a higher level of thermal expansion under the roller boundary constraint,
345 and corresponds to a lower initial normalized aperture value.

346 Besides, the aperture evolution behavior depends also on the initial reservoir temperature and the
347 relative configuration between in-situ stress directions and fracture orientation. The former effect can be
348 seen by comparing cases under different initial temperatures but the same reservoir stress condition (i.e.,
349 respective cases in different rows in Figures 6 and 7). When the initial reservoir temperature is increased
350 from 120 °C to 220 °C, the peak on the aperture evolution curve becomes higher, showing a larger aperture
351 variation. This temperature effect is more profound for the measured 110° fractures under the in-situ stress
352 condition of $k_x = 0.8$ and $k_y = 1.6$. In contrast, for the sampled 30° fractures, larger impacts occur when k_x
353 = 1.6 and $k_y = 0.8$. Similar effects of reservoir temperature can also be observed if the initial temperate is
354 further increased to 320 °C.

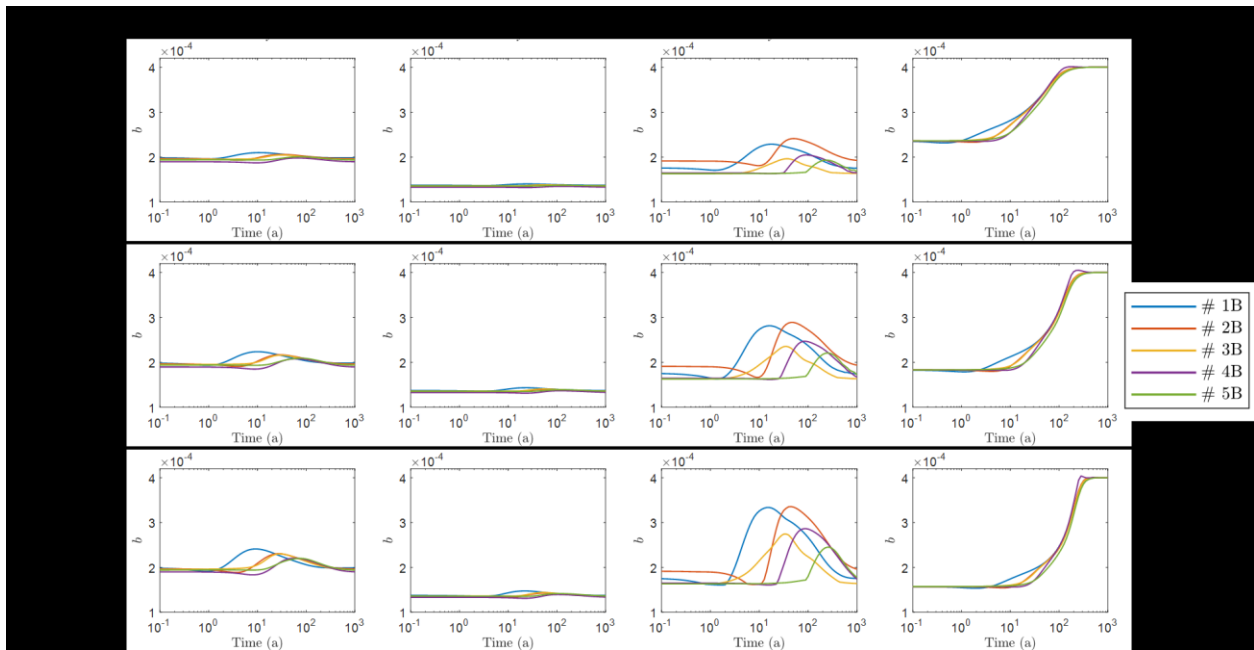


355

356

357

Figure 6. Aperture evolution of the five monitoring points for the 110° fracture set, under different in-situ stresses and reservoir initial temperatures.



358

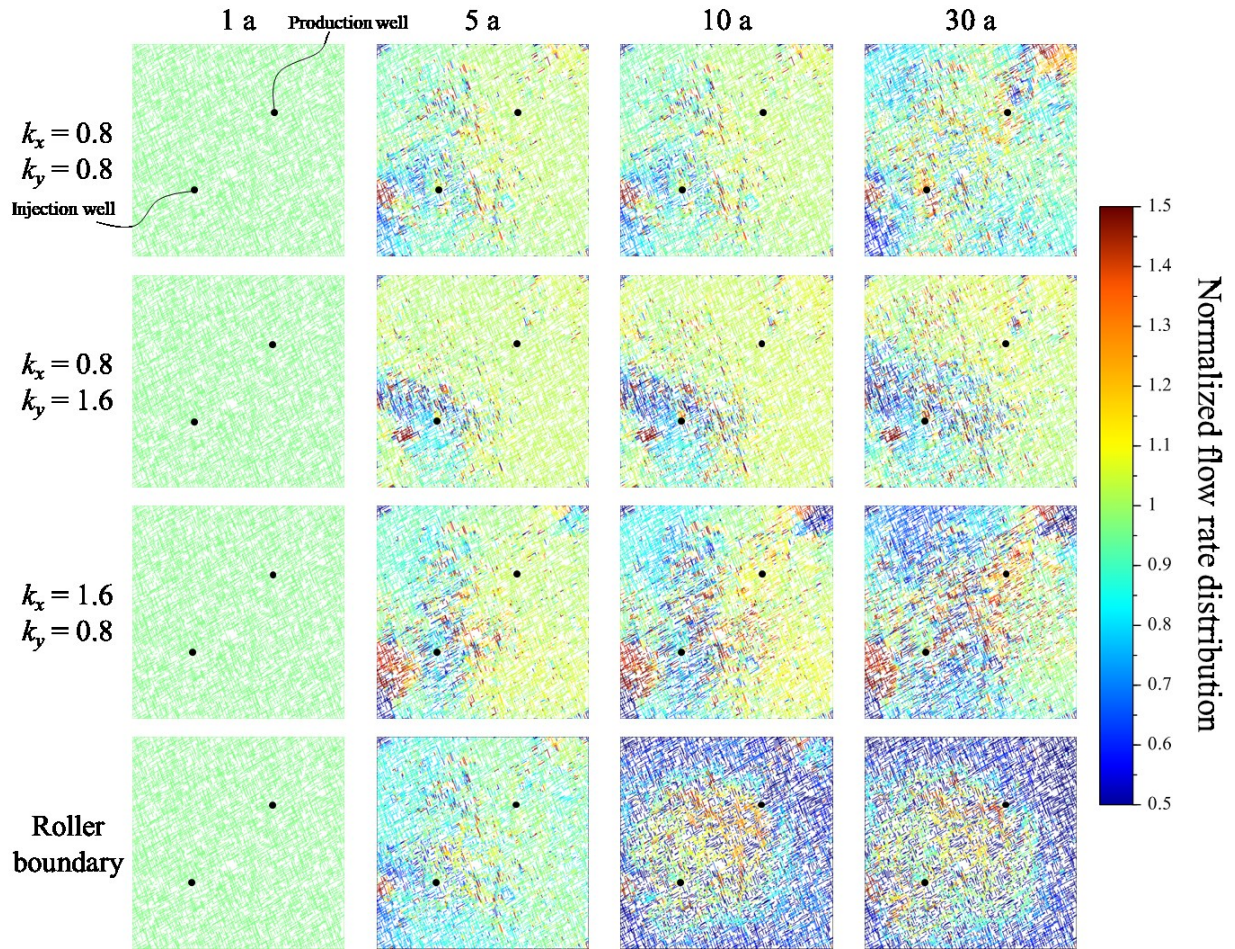
359

360

Figure 7. Aperture evolution at the five monitoring points for the 30° fracture set, under different in-situ stresses and reservoir initial temperatures.

361 4.2 Results of fluid flow

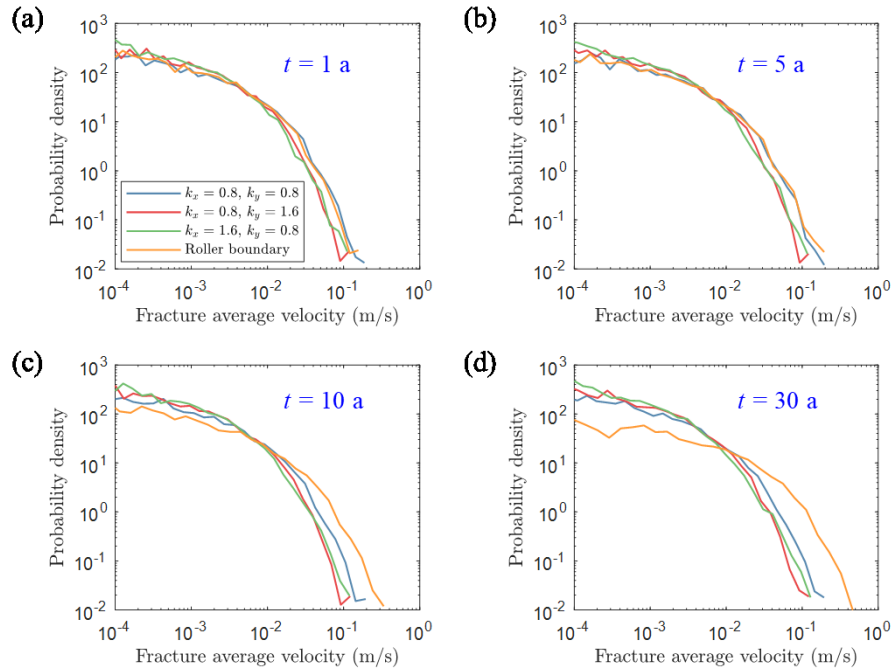
362 Figure 8 shows the evolution of normalized flow rate distributions for different in-situ stress cases but
363 the same initial temperature of $T_0 = 220$ °C. To facilitate the comparison, flow rate distributions are
364 normalized against the respective values at 1a. In the cases of the roller boundary, isotropic stress and
365 anisotropic stress with $k_x = 1.6$, $k_y = 0.8$, the flow rates along the mean flow direction seem to be enhanced
366 as the heat extraction proceeds. In contrast, in the case of $k_x = 0.8$, $k_y = 1.6$, flow rate enhancement occurs
367 mainly along fractures of the 110° set. This orientation dependency of flow is related to the shear dilation
368 effect of preferentially oriented fractures under anisotropic in-situ stresses. Figure 9 presents the
369 corresponding velocity PDFs at the four selected times (i.e. 1 a, 5 a, 10 a, and 30 a). At the initial production
370 phase, i.e., when $t = 1$ a, the isotropic stress loading and roller boundary cases have similar flow rate
371 distributions (Figure 9a), due to the similar aperture distributions (Figure 4). As the production time
372 increases, the two flow rate distributions become gradually different (Figures 9b, 9c and 9d). The velocity
373 distribution of the roller boundary case shifts towards large velocities, although the form of velocity scaling
374 (i.e., the PDF shape) remains unaltered. In contrast, the velocity distributions of the cases with in-situ stress
375 loadings change very slightly over time. In addition, the difference between the two anisotropic far-field
376 stress loadings is small and does not seem to change over time. This demonstrates the dominant role of in-
377 situ stresses in regulating the hydrological behavior of the fractured rock during the entire heat extraction
378 process.



379

380 **Figure 8.** Evolution of flow rate distribution when the reservoir initial temperature is $T_0 = 220^\circ$. Flow rates are normalized by the

381 mean flow rate of the respective 1a case.



382

383 **Figure 9.** Velocity PDFs for various in-situ stress cases at time (a) $t = 1$ a; (b) $t = 5$ a; (c) $t = 10$ a; (d) $t = 30$ a.

384

385

386

387

388

389

390

391

392

393

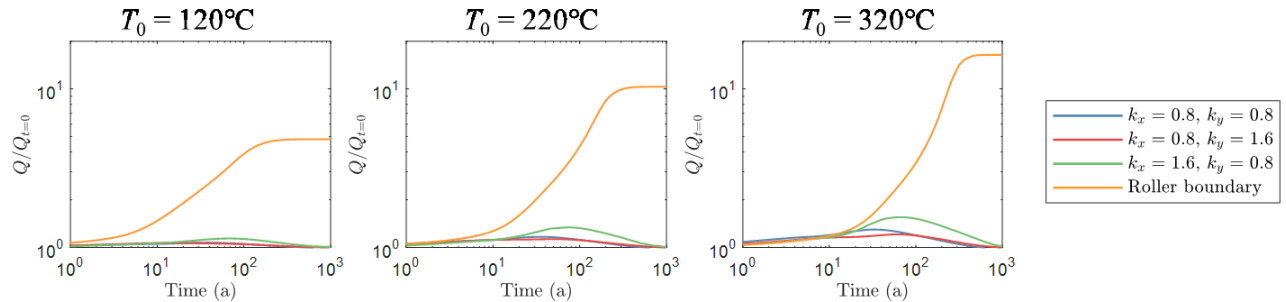
394

395

396

We further elucidate the bulk hydrological response of the fracture network under various conditions of in-situ stress and initial reservoir temperature. This is done by examining the production flow rate evolution are shown in Figure 10. Normalization is applied with respect to the flow rate at the beginning time of heat production. For a specific condition of initial temperature, the normalized production flow rate varies around 1 for cases where the fractured rock is subject to stress loading. This implies the flow rate does not change much during the heat production. All cases of stressed fracture networks have a similar variation trend of a first increase phase followed by a decline period; the normalized flow rate falls back to 1 at the end. The detailed variation behavior is controlled by the configuration of in-situ stresses. The variation of normalized flow rate is the largest in the stress case of $k_x = 1.6$ and $k_y = 0.8$ while it is the smallest when the far-field stress is rotated by 90° ; the flow rate variation of the isotropic stress case is in between the two anisotropic stress cases. It is also observed that an increase in the initial reservoir temperature results in an enhancement of the flow rate variation magnitude, while the general variation trend for different stress cases does not seem to change too much.

397 On the other hand, the roller boundary case behaves very differently. Similar to the evolution of
 398 apertures, there is a general increasing trend in flow rate over the entire production period. The rate of flow
 399 enhancement increases at first and then decreases. The total flow enhancement depends on the initial
 400 reservoir temperature, such that a higher initial temperature leads to a stronger flow enhancement.

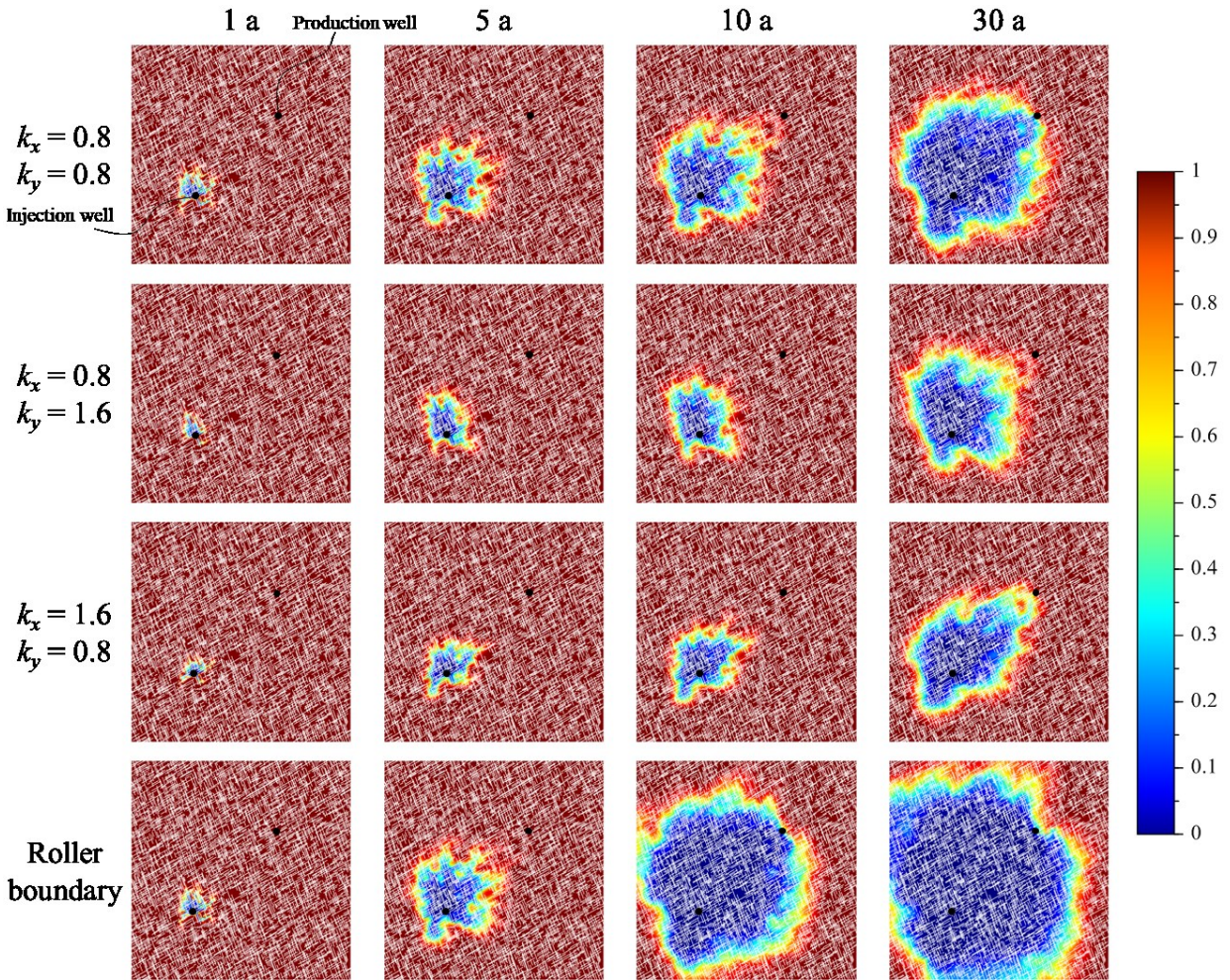


401
 402 **Figure 10.** Flow rate evolution at the production well for various in-situ stress and reservoir initial temperature cases.

403 4.3 Results of heat transfer

404 4.3.1 Spatial-temporal temperature distribution

405 Figure 11 displays the spatial distributions of reservoir temperature at times for various in-situ stress
 406 cases with an initial temperature of $T_0 = 220$ °C. At early times (e.g., at 1 a or 5 a), the difference in
 407 temperature distribution between the isotropic stress and roller boundary cases is small. As reservoir
 408 development proceeds (e.g., at 10 a and 30 a), the discrepancy between the distributions become gradually
 409 larger (Figure 11). The thermal front of the roller boundary case appears shaper and its arrival is earlier in
 410 comparison to that of the case under isotropic stress loading (i.e., when $k_x = k_y = 0.8$). On the contrary, if
 411 the fractured rock is loaded with anisotropic in-situ stresses, the thermal breakthrough at the production
 412 well is delayed comparing to the isotropic stress and roller boundary cases. However, coning of the thermal
 413 front is more apparent when $k_x = 1.6$ and $k_y = 0.8$, where the mean flow direction is in accordance with the
 414 preferentially oriented 30° fracture set accommodating shearing and dilation. The blunt thermal front shown
 415 in the case of $k_x = 0.8$ and $k_y = 1.6$ is due to the profound closure of fractures in the 30° set and relatively
 416 more opening of fractures in the 110° set.



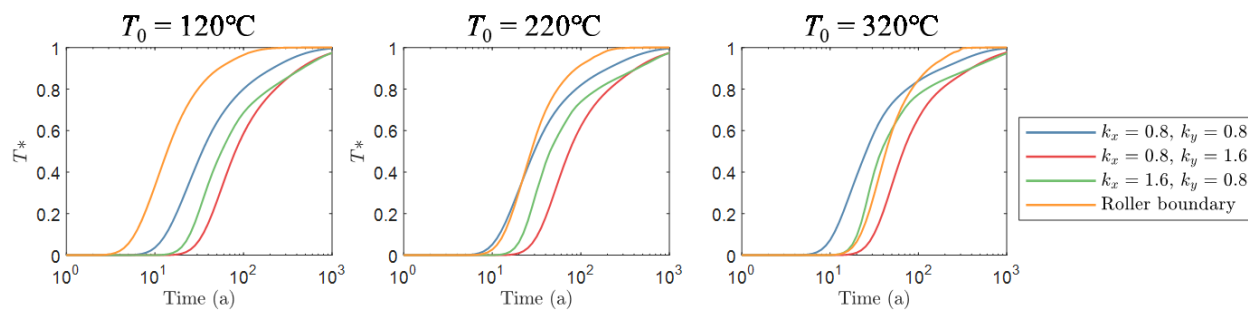
418

419 **Figure 11.** Evolution of normalized temperature distribution for various in-situ stress cases with 0 and 1 corresponding to T_m and
 420 T_0 . The reservoir initial temperature is $T_0 = 220^\circ\text{C}$.

421 4.3.2 Heat extraction performance

422 Figure 12 presents the variation of average outlet temperature for various stress cases and different
 423 initial reservoir temperature conditions. As the relative temperature T^* (defined by Eq. 13) varies from 0 to
 424 1, the temperature of extracted fluids varies from the initial rock temperature to that of injected fluids. If
 425 the fractured rock is isotropically stressed with $k_x = 0.8$ and $k_y = 0.8$, the onset time of T^* elevation for $T_0 =$
 426 120°C is delayed by more than five times compared to the roller boundary case, due to compression-
 427 induced aperture closures (Figure 12a). When anisotropic stresses are applied, the thermal breakthrough

428 becomes even later. The onset of T^* variation is slightly earlier in the stress case of $k_x = 1.6$ and $k_y = 0.8$,
 429 but the difference is much smaller than that between the isotropic and anisotropic stress cases. When the
 430 initial temperature is increased, the thermal breakthrough for the roller boundary case becomes strongly
 431 delayed, such that onset of T^* elevation occurs even later than that of the isotropic stress case, especially
 432 when the T_0 is increased to 320°C .



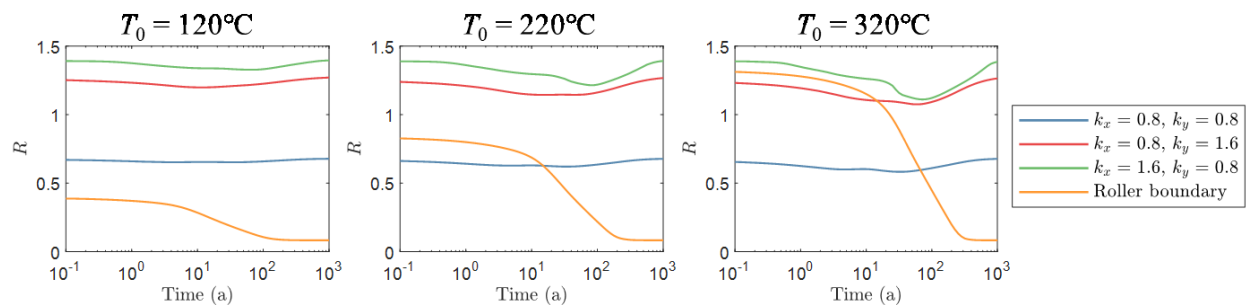
433
 434 **Figure 12.** Average temperature curves for various in-situ stress cases and reservoir initial temperature conditions.

435 To further elucidate the effect of in-situ stresses, we examine evolutionary behavior of the dimensionless
 436 number R (Eq. 14), which quantifies the relative timescales of convective and conductive heat transfer
 437 processes. The results are shown in Figure 13. In our recent study, we have shown that for a fixed reservoir
 438 operation configuration (e.g., reservoir size, average fracture spacing, initial temperature, distance between
 439 injection and production wells) R determines the ultimate heat extraction efficiency (Sun et al., 2020). A
 440 similar finding was also reported for heat transfer through single fractures (Martínez et al., 2014). In general,
 441 the heat transfer is limited by conduction when $R > 1$, while by convection when $R < 1$. Through numerous
 442 numerical simulations on a broad range of fracture network connectivity, it was found that, in general, for
 443 complex fracture networks, the highest heat extraction efficiency occurs in the vicinity of $R = 1$ (Sun et al.,
 444 2020). Also, for $R < 1$ the gradient of heat extraction efficiency variation is much higher.

445 The R values of all our simulations are within the range of $R < 1.5$, implying the heat transfer process
 446 of the simulations are within the convection-dominated regime. Note that the R is calculated based on all
 447 fractures in the domain so that the value of R will be overestimated. For the main flow channels controlling

448 the heat production performance, R is much smaller. When $T_0 = 120$ °C, the stress boundary cases show a
 449 small variation in R over the entire heat extraction process (Figure 13a). The two anisotropic in-situ cases
 450 have a similar R value (~ 1.4), which is about two times higher than that of the isotropic stress case (~ 0.7).
 451 In contrast, the roller boundary case exhibits a large R variation but a much lower value. The R value starts
 452 to decrease from the initial value of about 0.1 at around 1 a and becomes stabilized again at $R = 0.08$ after
 453 40 a.

454 If the initial reservoir temperature is increased, the R values of the stressed fracture networks only
 455 show a slightly increased variation magnitude comparing to the results at $T_0 = 120$ °C (Figures 13b and
 456 13c). For the roller boundary case, the initial R value is significantly increased, although it will drop to the
 457 same level eventually. The initial R value is determined by the temperature level: a higher initial
 458 temperature corresponds to a higher initial R value. When $T_0 = 320$ °C, the R of the isotropic in-situ stress
 459 case is initially higher than that of the roller boundary case, but the R value drops fast and eventually
 460 becomes much lower. This observation suggests that without considering the in-situ stress effect, numerical
 461 simulation may unrealistically predict that an initially efficient system tends to become inefficient within a
 462 short time of less than 10 years.



463
 464 **Figure 13.** Evolution of R for various in-situ stress and reservoir initial temperature cases.

465 5. Discussions and Conclusions

466 In this study, we have shown how the interplay between thermal and in-situ stresses controls the heat
 467 transfer behavior in 2D fractured reservoirs. The in-situ stresses tend to suppress fracture apertures and
 468 regulate the fluid flow within fracture networks. The effects of in-situ stress on the transient heat transfer
 469 have been demonstrated by the evolution of fracture aperture and velocity statistics. Neglecting the in-situ

470 stress effect, the aperture PDF shifts towards large values as the thermal front propagates from the injection
471 well towards the production well at the downstream. For anisotropic in-situ stresses, an important
472 observation is that the transient cooling may trigger fracture shear dilations. Significant shear dilations
473 occur along the fracture set that is preferentially oriented with respect to the maximum principle stress.
474 Such an important geomechanical effect has not been explored in previous THM modelling studies of
475 fractured geothermal reservoirs (Sun et al., 2017; Yao et al., 2018).

476 Another important insight from our simulations is that the aperture evolution of a fracture during heat
477 extraction may be controlled by two mechanisms: 1) aperture enlargement due to transient cooling upon
478 the arrival of thermal front at the fracture, which have been discussed extensively in the past (Ghassemi &
479 Zhou, 2011; Hicks et al., 1996; Salimzadeh et al., 2018); 2) aperture reduction caused by a stress disturbance
480 transmitted from a stress redistribution process at a remote location experiencing cooling, i.e., before the
481 thermal front propagates to the location of the fracture. The second mechanism is relevant not only to the
482 optimization of heat extraction efficiency as demonstrated in the current paper, but also to the risk
483 management of induced seismicity by fluid injection during the heat production. Our simulations suggest
484 that a stress perturbation caused by cooling may enhance the probability of activating a geological structure,
485 e.g. pre-existing faults, located remotely. This only occurs when the in-situ stress effect is properly
486 modelled in the simulation (Figures 6 and 7). The remote triggering phenomena of seismicity have been
487 identified in several field observations (Ellsworth, 2013; van der Elst et al., 2013). The present study will
488 be further extended to quantitatively investigate how the interaction among thermal, hydraulic and
489 geomechanical processes influences induced seismicity in terms of magnitude and spatial extent in the
490 future.

491 We have compared the THM behaviors of fractured rocks under stress boundary constraints with that
492 with zero-displacement boundary constraints (i.e., roller boundaries). In previous THM modeling studies
493 of fractured geothermal reservoirs, the roller boundary condition is the most popular numerical boundary
494 type that has been adopted for simulating the geological confinement imposed by surrounding rocks. In
495 contrast, the stress boundary constraints are seldomly used (Han et al., 2019). We suggest that the stress

496 boundary constraints may be closer to the actual condition of subsurface geothermal reservoirs. Our results
497 have shown that in a coupled THM model with all external boundaries applied with the roller boundary
498 condition, the fracture apertures increase continuously over the entire production phase. Also, the predicted
499 spatial variation of apertures is very small. These behaviors tend to be unrealistic for real fracture systems
500 at great depth.

501 Our study highlights the critical importance of incorporating the geomechanical stresses in modeling
502 of heat transfer and geothermal performance. The traditional approaches that ignore the effects of reservoir
503 in-situ stress state may lead to an overestimation of fracture aperture increase and heat extraction. The
504 efficiency of heat extraction declines much earlier and fast when the in-situ stress effect is omitted. The
505 findings in this study have important implications for designing efficient operation scheme for geothermal
506 reservoirs as well as for managing seismic hazards from fluid injections. However, we admit that there are
507 still some limitations. First, this work did not consider shear induced fracture propagation. This may not
508 affect the general observations and conclusions in this paper, since the connectivity of the natural fracture
509 network is high whereas the stress ratio is low (≤ 2) such that the system is away from the critically-
510 stressed state (Zoback, 2007). The effect of new crack formation may become dominant for fracture
511 networks close to the percolation threshold and subject to high stress ratios (Jiang et al., 2019). Furthermore,
512 the current study is based on 2D fracture systems. Efforts are need to extend the THM model to study the
513 potentially important 3D effects.

514 **Acknowledgements**

515 Zhixue Sun is grateful for the funding from the National Natural Science Foundation of China (Grant
516 NO.51774317), the Fundamental Research Funds for the Central Universities (Grant No.18CX02100A)
517 and the China Scholarship Council Fund. Xiaoguang Wang was funded by PRC-CNRS Joint Research
518 Project from the National Natural Science Foundation of China (Grant No. 5181101856) and National Key

519 Research and Development Program of China (Grant No. 2020YFC1808300). Wen Zhou is grateful for
520 research grants from National Natural Science Foundation of China (Grant No. 42002157 and 41972137).
521 The authors are grateful for the constructive comments from the editor and two anonymous reviewers,
522 which helped to improve the quality of the paper.

523 **References**

- 524 Bai, T., Pollard, D. D., & Gao, H. (2000). Explanation for fracture spacing in layered materials. *Nature*,
525 *403*(6771), 753–756.
- 526 Bandis, S., Lumsden, A., & Barton, N. (1983). Fundamentals of rock joint deformation. In *International*
527 *Journal of Rock Mechanics and Mining Sciences & Geomechanics Abstracts* (Vol. 20, pp. 249–
528 268). Pergamon.
- 529 Barton, N., Bandis, S., & Bakhtar, K. (1985). Strength, deformation and conductivity coupling of rock
530 joints. In *International journal of rock mechanics and mining sciences & geomechanics abstracts*
531 (Vol. 22, pp. 121–140). Elsevier.
- 532 COMSOL Multiphysics®. (2018). (Version v. 5.4). Stockholm, Sweden: COMSOL AB. Retrieved from
533 www.comsol.com
- 534 Einstein, H. H., & Baecher, G. B. (1983). Probabilistic and statistical methods in engineering geology. *Rock*
535 *Mechanics and Rock Engineering*, *16*(1), 39–72.
- 536 Ellsworth, W. L. (2013). Injection-Induced Earthquakes. *Science*, *341*(6142), 1225942–1225942.
- 537 van der Elst, N. J., Savage, H. M., Keranen, K. M., & Abers, G. A. (2013). Enhanced Remote Earthquake
538 Triggering at Fluid-Injection Sites in the Midwestern United States. *Science*, *341*(6142), 164–167.
539 <https://doi.org/10.1126/science.1238948>
- 540 Fu, P., Hao, Y., Walsh, S. D. C., & Carrigan, C. R. (2016). Thermal Drawdown-Induced Flow Channeling
541 in Fractured Geothermal Reservoirs. *Rock Mechanics and Rock Engineering*, *49*(3), 1001–1024.
- 542 Gan, Q., & Elsworth, D. (2016). Production optimization in fractured geothermal reservoirs by coupled
543 discrete fracture network modeling. *Geothermics*, *62*, 131–142.

544 Ghassemi, A., & Zhou, X. (2011). A three-dimensional thermo-poroelastic model for fracture response to
545 injection/extraction in enhanced geothermal systems. *Geothermics*, 40(1), 39–49.

546 Guo, B., Fu, P., Hao, Y., Peters, C. A., & Carrigan, C. R. (2016). Thermal drawdown-induced flow
547 channeling in a single fracture in EGS. *Geothermics*, 61, 46–62.

548 Han, S., Cheng, Y., Gao, Q., Yan, C., Han, Z., & Zhang, J. (2019). Investigation on heat extraction
549 characteristics in randomly fractured geothermal reservoirs considering thermo-poroelastic effects.
550 *Energy Science & Engineering*, 7(5), 1705–1726.

551 Hicks, T. W., Pine, R. J., Willis-Richards, J., Xu, S., Jupe, A. J., & Rodrigues, N. E. V. (1996). A hydro-
552 thermo-mechanical numerical model for HDR geothermal reservoir evaluation. *International*
553 *Journal of Rock Mechanics and Mining Sciences & Geomechanics Abstracts*, 33(5), 499–511.
554 [https://doi.org/10.1016/0148-9062\(96\)00002-2](https://doi.org/10.1016/0148-9062(96)00002-2)

555 Hudson, J. A., & Priest, S. D. (1983). Discontinuity frequency in rock masses. *International Journal of*
556 *Rock Mechanics and Mining Sciences & Geomechanics Abstracts*, 20(2), 73–89.

557 Jaeger, J. C., Cook, N. G., & Zimmerman, R. (2009). *Fundamentals of rock mechanics*. John Wiley & Sons.

558 Jiang, C., Wang, X., Sun, Z., & Lei, Q. (2019). The Role of In Situ Stress in Organizing Flow Pathways in
559 Natural Fracture Networks at the Percolation Threshold. *Geofluids*, 2019, 1–14.
560 <https://doi.org/10.1155/2019/3138972>

561 Koh, J., Roshan, H., & Rahman, S. S. (2011). A numerical study on the long term thermo-poroelastic effects
562 of cold water injection into naturally fractured geothermal reservoirs. *Computers and Geotechnics*,
563 38(5), 669–682.

564 Lei, Q., Latham, J.-P., & Xiang, J. (2016). Implementation of an Empirical Joint Constitutive Model into
565 Finite-Discrete Element Analysis of the Geomechanical Behaviour of Fractured Rocks. *Rock*
566 *Mechanics and Rock Engineering*, 49(12), 4799–4816. [https://doi.org/10.1007/s00603-016-1064-](https://doi.org/10.1007/s00603-016-1064-3)
567 3

568 Lei, Q., Wang, X., Xiang, J., & Latham, J.-P. (2017). Polyaxial stress-dependent permeability of a three-
569 dimensional fractured rock layer. *Hydrogeology Journal*, 25(8), 2251–2262.
570 <https://doi.org/10.1007/s10040-017-1624-y>

571 Martínez, Á. R., Roubinet, D., & Tartakovsky, D. M. (2014). Analytical models of heat conduction in
572 fractured rocks. *Journal of Geophysical Research: Solid Earth*, 119(1), 83–98.
573 <https://doi.org/10.1002/2012JB010016>

574 Pandey, S. N., & Vishal, V. (2017). Sensitivity analysis of coupled processes and parameters on the
575 performance of enhanced geothermal systems. *Scientific Reports*, 7(1), 17057.
576 <https://doi.org/10.1038/s41598-017-14273-4>

577 Pruess, K., & Narasimhan, T. N. (1985). A Practical Method for Modeling Fluid and Heat Flow in Fractured
578 Porous Media. *Society of Petroleum Engineers Journal*, 25(01), 14–26.

579 Rahman, M., Hossain, M., & Rahman, S. (2002). A shear-dilation-based model for evaluation of
580 hydraulically stimulated naturally fractured reservoirs. *International Journal for Numerical and*
581 *Analytical Methods in Geomechanics*, 26(5), 469–497.

582 Renshaw, C. E., & Park, J. C. (1997). Effect of mechanical interactions on the scaling of fracture length
583 and aperture. *Nature*, 386(6624), 482–484. <https://doi.org/10.1038/386482a0>

584 Renshaw, Carl E, & Pollard, D. D. (1994). Numerical simulation of fracture set formation: A fracture
585 mechanics model consistent with experimental observations. *Journal of Geophysical Research*, 99,
586 9359–9372.

587 Rives, T., Razack, M., Petit, J., & Rawnsley, K. (1992). Joint spacing: analogue and numerical simulations.
588 *Journal of Structural Geology*, 14(8), 925–937.

589 Saeb, S., & Amadei, B. (1992). Modelling rock joints under shear and normal loading. *International*
590 *Journal of Rock Mechanics and Mining Sciences & Geomechanics Abstracts*, 29(3), 267–278.
591 [https://doi.org/10.1016/0148-9062\(92\)93660-C](https://doi.org/10.1016/0148-9062(92)93660-C)

592 Salimzadeh, S., Paluszny, A., Nick, H. M., & Zimmerman, R. W. (2018). A three-dimensional coupled
593 thermo-hydro-mechanical model for deformable fractured geothermal systems. *Geothermics*, *71*,
594 212–224.

595 Sun, Z., Zhang, X., Xu, Y., Yao, J., Wang, H., Lv, S., et al. (2017). Numerical simulation of the heat
596 extraction in EGS with thermal-hydraulic-mechanical coupling method based on discrete fractures
597 model. *Energy*, *120*, 20–33.

598 Sun, Z., Jiang, C., Wang, X., Lei, Q., & Jourde, H. (2020). Joint influence of in-situ stress and fracture
599 network geometry on heat transfer in fractured geothermal reservoirs. *International Journal of Heat
600 and Mass Transfer*, *149*, 119216.

601 Ucar, E., Berre, I., & Keilegavlen, E. (2017). Postinjection normal closure of fractures as a mechanism for
602 induced seismicity. *Geophysical Research Letters*, *44*(19), 9598–9606.

603 Vik, H. S., Salimzadeh, S., & Nick, H. M. (2018). Heat Recovery from Multiple-Fracture Enhanced
604 Geothermal Systems: The Effect of Thermoelastic Fracture Interactions. *Renewable Energy*, *121*,
605 606–622.

606 Wang, S., Huang, Z., Wu, Y., Winterfeld, P. H., & Zerpa, L. E. (2016). A semi-analytical correlation of
607 thermal-hydraulic-mechanical behavior of fractures and its application to modeling reservoir scale
608 cold water injection problems in enhanced geothermal reservoirs. *Geothermics*, *64*, 81–95.

609 Wang, X., Lei, Q., Lonergan, L., Jourde, H., Gosselin, O., & Cosgrove, J. (2017). Heterogeneous fluid flow
610 in fractured layered carbonates and its implication for generation of incipient karst. *Advances in
611 Water Resources*, *107*, 502–516. <https://doi.org/10.1016/j.advwatres.2017.05.016>

612 Wu, H., & Pollard, D. D. (1995). An experimental study of the relationship between joint spacing and layer
613 thickness. *Journal of Structural Geology*, *17*(6), 887–905.

614 Wu, Y. S. (1999). On the Effective Continuum Method for Modeling MultiphaseFlow, Multicomponent
615 Transport and Heat Transfer in FracturedRock. *Office of Scientific & Technical Information
616 Technical Reports*, *122*, 299–312.

- 617 Yao, J., Zhang, X., Sun, Z., Huang, Z., Liu, J., Li, Y., et al. (2018). Numerical simulation of the heat
618 extraction in 3D-EGS with thermal-hydraulic-mechanical coupling method based on discrete
619 fractures model. *Geothermics*, 74, 19–34. <https://doi.org/10.1016/j.geothermics.2017.12.005>
- 620 Zhao, Y., Feng, Z., Feng, Z., Yang, D., & Liang, W. (2015). THM (Thermo-hydro-mechanical) coupled
621 mathematical model of fractured media and numerical simulation of a 3D enhanced geothermal
622 system at 573 K and buried depth 6000–7000 M. *Energy*, 82, 193–205.
- 623 Zoback, M. D. (2007). *Reservoir Geomechanics*. Cambridge University Press.